JOURNAL OF PROPULSION AND POWER
Vol. 18, No. 5, September–October 2002

Turbomachine Blade Row Interaction Predictions with a Three-Dimensional Finite Element Method

Dana A. Gottfried* and Sanford Fleeter†
Purdue University, West Lafayette, Indiana 47907

High-cycle fatigue (HCF) is a key issue for the advancement of gas-turbine performance and endurance. Models simulating the cyclic aerodynamic forces experienced by gas-turbine vanes are necessary to make quantitative predictions of HCF during design. Although such models exist, there is an urgent need to compare them with benchmark data to assess their accuracy and reliability. In this study, TAM-ALE3D is utilized to simulate the inlet guide vane (IGV) and rotor blade rows in the Purdue Transonic Compressor at both part-speed and design-speed conditions. Of particular interest is the unsteady flow in the IGV row generated by the part-speed potential field and the design-speed shock system generated by the downstream rotor. To assess the accuracy of the TAM-ALE3D predictions, the 90% span instantaneous IGV vane-to-vane flowfield and vane surface pressures are correlated with appropriate state-of-the-art data.

Nomenclature

A	=	sound speed
a	=	acceleration
b	=	body force per mass
E	=	energy per mass
F^{hg}	=	hourglass resisting force
ℓ	=	length scale
m	=	mass
n	=	unit normal pointing outward
P	=	pressure
q	=	shock smearing factor
S	=	surface area
t	=	time
u	=	velocity
$\mathcal{V}$	=	volume
x	=	spatial coordinate
γ	=	ratio of specific heats
ρ	=	density
ω	=	rotational speed

Subscripts

av	=	time-averaged value
i	=	three coordinate directions

Superscripts

ext	=	extrapolated from interior
n	=	time level
*	=	center of advected volume
$'$	=	node-centered control volume

Introduction

HIGH-CYCLE fatigue (HCF) is a critical concern in designing turbomachinery for reliability and is, thus, a key technology development issue. Currently, designers address HCF issues with a computational fluid dynamics (CFD) analysis of a single blade row, with the unsteady forcing due to prespecified inflow/outflow boundary conditions or the blade motion itself. The resulting blade row unsteady loading is then utilized with a blade finite element model to determine the unsteady stresses, with these unsteady stresses being either too high or acceptable based on fatigue life expectations. In this whole process, the inadequate modeling of blade row coupling effects in the CFD analysis may be the cause for a number of surprise HCF failures.

To address the HCF problem, analysis tools are necessary to simulate the unsteady flow environment within multistage blade rows. Such simulation tools must model blade row coupling and interaction effects directly and also be validated with appropriate benchmark data. Several multistage turbomachinery unsteady aerodynamic analyses have been developed, for example, TURBO[1,2] and ADPAC,[3] both of which are finite volume schemes.

The model of interest therein is TAM-ALE3D, a three-dimensional Euler solver using a finite element scheme. Validation of TAM-ALE3D for modeling the unsteady aerodynamics of a single blade row has been presented.[4] Such high-level multistage turbomachinery analyses begin to meet the need for HCF design tools. However, before being incorporated into design systems, these analyses must be validated with benchmark data.

This paper addresses the need to validate the new TAM-ALE3D multistage analysis with benchmark data. This is accomplished through a TAM-ALE3D Euler simulation of the inlet guide vane (IGV)–rotor unsteady aerodynamic interactions performed on a parallel computing platform for both transonic and subsonic rotor conditions. The IGV and rotor blade passages are processed on two CPUs, with message passing interface routines used for communication between the two domains. The results of this simulation are correlated with corresponding benchmark data, including both 90% span IGV surface steady and unsteady pressures and the IGV passage flowfield.

Mathematical Model

The equations stating conservation of mass, momentum, and energy are marched forward in time, with the physical domain discretized by an unstructured assembly of finite elements. These elements are not required to move with the material, nor must they remain stationary, making the scheme an arbitrary Lagrangian Eulerian scheme. For each step forward in time, there are three distinct calculation procedures: 1) the Lagrange calculation, 2) the mesh relaxation, and 3) the advection calculation.

Received 5 July 2001; revision received 20 February 2002; accepted for publication 21 February 2002.

*Postdoctoral Researcher, School of Mechanical Engineering; gottfrie@purdue.edu. Member AIAA.

†McAllister Distinguished Professor, School of Mechanical Engineering; fleeter@purdue.edu. Fellow AIAA.

Lagrange Calculation

The elements move with the material with no flux of mass or energy through the element faces in the Lagrange calculation. Thus, conservation of mass requires that the mass of the elements be constant during this calculation. Conservation of momentum is

$$\frac{\mathrm{D}}{\mathrm{D}t}\int_{\mathcal{V}} \rho u_i \,\mathrm{d}\mathcal{V} = -\int_S (P+q) n_i \,\mathrm{d}S + \int_{\mathcal{V}} \rho b_i \,\mathrm{d}\mathcal{V} \tag{1}$$

where summation notation is used, with i representing the three coordinate directions and where $\mathrm{D}/\mathrm{D}t$ is the material derivative showing that the control volume moves with the material.

The term q is a mathematical device that smears shocks over distances comparable to the mesh interval. The form of q used here is that proposed by Noh[5]:

$$q = \begin{cases} -C_0 \rho \ell^2 |u_{i,i}| u_{i,i} - C_1 \ell \rho A u_{i,i} & \text{if} \quad u_{i,i} < 0 \\ 0 & \text{if} \quad u_{i,i} \geq 0 \end{cases} \tag{2}$$

where ℓ is a length on the order of the mesh interval, C_0 is the quadratic q coefficient ($\sim$1), and C_1 is the linear q coefficient ($\sim$1). The comma in the subscript of u denotes differentiation, so that $u_{i,i}$ represents the divergence of the velocity.

To discretize Eq. (1), the integration volumes are taken to be the finite elements. Physical quantities are assigned to staggered locations in the element. Velocities and accelerations are stored at the nodes (vertices) and are assumed to vary linearly over the element. The pressure, energy, and q term are stored at the center and are constant over the element. The element mass is stored at both the center and element nodes, with the nodal mass being one-eighth of the sum of the surrounding element masses.

In the time discretization, the velocities and the q terms are taken at half time levels, denoted by superscript $n \pm \frac{1}{2}$, whereas all other quantities are evaluated at full time levels. Evaluating the velocities and q terms at half time levels produces difference equations that are centered in space and are, thus, second-order accurate.[5] The body force per unit mass b_i is required to account for Coriolis and centripetal accelerations in a rotating reference frame. For a constant angular velocity ω along the three-axis (i.e., the engine centerline for this analysis), the body force per unit mass is

$$b_1^n = \left(x_1^n \omega + 2u_2^{n-\frac{1}{2}}\right)\omega, \qquad b_2^n = \left(x_2^n \omega - 2u_1^{n-\frac{1}{2}}\right)\omega, \qquad b_3^n = 0 \tag{3}$$

In Eq. (1), the density of the volume is constant in space and time, and so the left-hand side is the product of mass and acceleration. Because acceleration is stored at the element nodes, it is convenient to discretize Eq. (1) by using a node-centered element. The pressure and q term acting on the surfaces of this element are considered in the evaluation of the surface integral of Eq. (1). In discretized form, Eq. (1) is

$$a_i^n = \frac{1}{m'^n} \sum_e \left(P^n - q^{n-\frac{1}{2}}\right) n_i' \Delta S' + b_i^n + \frac{1}{m'^n} F_i^{\mathrm{hg}} \tag{4}$$

where m' is the mass of a node, n_i' and $\Delta S'$ are the outward normal and surface area of the node-centered element contained within element e, and the subscript e on the summation denotes summation over all of the elements surrounding the node, eight elements for an interior node or four, two, or one element for a boundary node. The F_i^{hg} term represents the hourglass viscous force required to damp the hourglass modes.[6]

After the nodal acceleration is found from Eq. (4), a centered-difference formula is used to find the velocity at time level $n+\frac{1}{2}$. The centered-difference formula is again applied to the velocity to find the new position of the node at time level $n+1$:

$$u_i^{n+\frac{1}{2}} = u_i^{n-\frac{1}{2}} + a_i^n \Delta t \tag{5}$$

$$x_i^{n+1} = x_i^n + u_i^{n+\frac{1}{2}} \Delta t \tag{6}$$

where Δt is held fixed throughout the simulation and is chosen small enough to satisfy the Lagrangian time-step restriction and advection time-step restriction in all domains.[7]

Using energy conservation to update the elemental energy completes the Lagrange step. For a control volume with no energy flux through its faces, energy conservation is

$$\frac{\mathrm{D}}{\mathrm{D}t}\int_{\mathcal{V}} \rho E \,\mathrm{d}\mathcal{V} = -\int_{\mathcal{V}} (P+q) u_{i,i} \,\mathrm{d}\mathcal{V} \tag{7}$$

The average velocity divergence of a finite element is the nondimensional rate of change of volume of the element, that is, $(1/\mathcal{V})(\mathrm{D}\mathcal{V}/\mathrm{D}t)$. Substituting this for $u_{i,i}$ and substituting the equation of state for a fluid for P gives

$$\frac{\mathrm{D}\rho E\mathcal{V}}{\mathrm{D}t} = -[(\gamma-1)\rho E + q]\frac{\mathrm{D}\mathcal{V}}{\mathrm{D}t} \tag{8}$$

If q were zero, this could be integrated in closed form. However, because q is not necessarily zero, a third-order Runge–Kutta method is used to integrate this to find the elemental energy at time level $n+1$.

Mesh Relaxation

In the Lagrange calculation, the elements change position according to Eq. (6). Clearly, the fluid elements cannot continue moving in a Lagrangian fashion; otherwise the solution will be destroyed as the elements exit the solution domain. Therefore, before proceeding to the next time step, it is necessary to relax the finite element mesh to a new position and calculate new elemental and nodal quantities via an advection calculation. In this study, solid boundaries such as blades and vanes are not moving. Thus, mesh relaxation is accomplished with a straightforward placement of the elements back to their original position at the beginning of the Lagrange step.

Advection Calculation

As an element moves from its position at the end of the Lagrange calculation to its new position after mesh relaxation, there is a flux of mass, momentum, and energy through the six faces of the element. The mass, momentum, and energy of the element are updated by simply summing the flux of these quantities through the element faces.

Consider a single face of an element that moves from its old position to its new position after mesh relaxation. The volume between the old and new face positions, termed the face-swept volume and denoted by $\Delta\mathcal{V}_f$, is positive if the face moves into the element. The change in mass, momentum, and energy of the element is then

$$\Delta m = -\sum_{j=1}^{6} \left(\rho^* \Delta\mathcal{V}_f\right)_j \tag{9}$$

$$\Delta(m'u_i) = -\sum_{j'=1}^{6} \left[(\rho u_i)^* \Delta\mathcal{V}_f'\right]_{j'} \tag{10}$$

$$\Delta(mE) = -\sum_{j=1}^{6} \left[(\rho E)^* \Delta\mathcal{V}_f\right]_j \tag{11}$$

where the summation is over the six faces of the element.

The starred quantities in Eqs. (9–11) are the values at the center of the face-swept volume and are determined with a second-order upwinding scheme. The scheme requires information from the two elements upwind of the face and the one element downwind of the face. Monotonic limiters[7] are employed to assure that the starred quantities are never greater or less than the corresponding quantities in the upwind and downwind elements. The momentum advection calculation of Eq. (10) is performed with the node-centered element because the velocities are stored at the element nodes.

Boundary Conditions

Airfoil Surface Boundary

The airfoils are modeled with immovable shell elements. At the end of both the Lagrange and advection calculations, the fluid nodes adjacent to the airfoils could be away from the surface due to airfoil curvature. They are, thus, projected normally onto the airfoil at the end of these two calculations. In addition, at the end of both calculations, the velocity of the nodes next to the airfoil is made tangent to the surface.

Periodic Boundaries

Only one airfoil passage is analyzed for each domain, with the flow variables transferred directly between the airfoil-to-airfoil boundaries. This corresponds to a 0-deg interblade phase angle.

Hub and Tip Boundaries

The hub and tip cylindrical surfaces of the domain are slip surfaces. At the end of the Lagrange and advection calculations, the nodes next to the hub and tip surfaces are projected normally onto these surfaces and their velocities made tangent.

Inflow and Outflow Boundaries

During the Lagrange calculation, the exit static pressure and inflow velocity are specified. The exit static pressure is included in the force summation of Eq. (4) for those nodes on the outflow boundary. For inflow, the velocities calculated by Eq. (5) are ignored and overwritten by the specified inflow velocity.

As the mesh is relaxed after each Lagrange step, the inflow boundary moves into the region upstream of the domain. Consequently, the advection step requires the specification of two other boundary conditions at inflow, namely, ρ^* and $(\rho E)^*$. The momentum flux $(\rho u_i)^*$ at inflow is deduced from the inflow velocity defined earlier.

To minimize reflections at the inflow and outflow boundaries, one-dimensional partially nonreflecting unsteady boundary conditions are used.[8] The inflow boundary is made nonreflecting by adding the following perturbations to the specified inflow:

$$\Delta\rho^{\text{inflow}} = -\frac{\rho_{\text{av}}\Delta u_3^{\text{ext}}}{2A_{\text{av}}} + \frac{\Delta P^{\text{ext}}}{2A_{\text{av}}^2} \tag{12}$$

$$\Delta u_3^{\text{inflow}} = \frac{\Delta u_3^{\text{ext}}}{2} - \frac{\Delta P^{\text{ext}}}{2\rho_{\text{av}}A_{\text{av}}} \tag{13}$$

$$\Delta(\rho E)^{\text{inflow}} = (\gamma - 1)\left[-\frac{\rho_{\text{av}}A_{\text{av}}\Delta u_3^{\text{ext}}}{2} + \frac{\Delta P^{\text{ext}}}{2}\right] \tag{14}$$

where superscript ext indicates that this perturbation quantity is extrapolated from the interior adjacent to the inflow boundary.

At the outflow boundary, the specified pressure is perturbed with

$$\Delta P^{\text{outflow}} = \rho_{\text{av}}A_{\text{av}}\Delta u_3^{\text{ext}}/2 + \Delta P^{\text{ext}}/2 \tag{15}$$

where the time-averaged pressure at outflow is user-specified, but the other outflow time-averaged quantities are calculated as part of the solution.

Parallel Computations

Parallel computations are performed by placing a domain from each airfoil row, that is, the IGV and the rotor, on a processor. For rows with equal airfoil counts, the situation of this study, this domain is a single passage. To simplify the interpolation between domains, there are equal numbers of element faces on the interface. In addition, the tangential and radial spacings of these element faces on the interface are constant.

Because the domains are rotating relative to each other, linear interpolation in the tangential direction is used to pass information between domains. Because the mesh geometry at the interface is the same between the two domains and because flow quantities vary linearly (velocity) or are constant (density, energy, etc.) over an element, linear interpolation is sufficient to pass information between domains accurately.

The philosophy of the interface boundary treatment is that, whatever information an interior calculation requires, the same information is provided for the same calculation at the interface. The interface nodes and elements, thus, behave in a transparent manner, that is, as if the interface between domains does not exist.

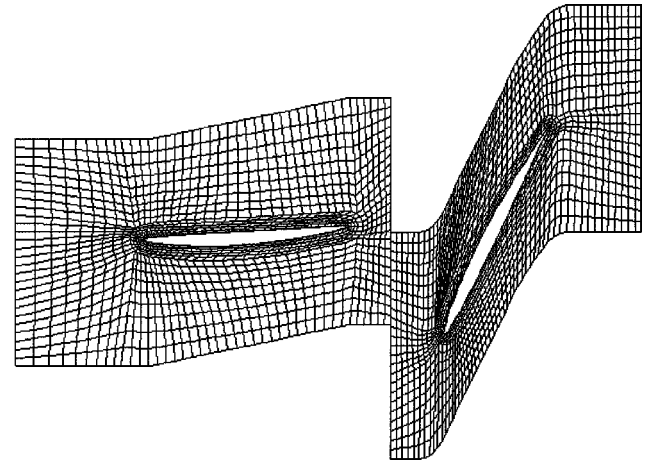

Fig. 1 Finite element meshes for IGV and rotor passage tip sections.

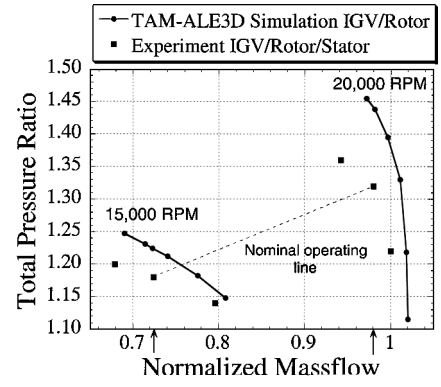

Fig. 2 Performance map.

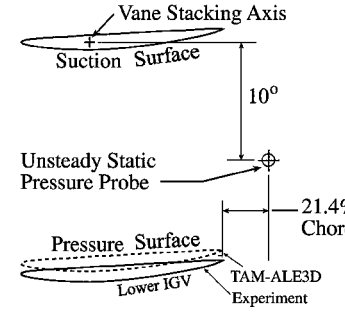

Fig. 3 IGV passage and unsteady static pressure probe locations.

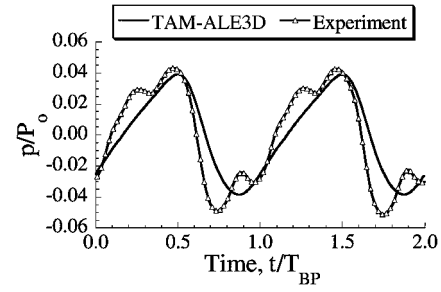

Fig. 4 Rotor-generated forcing function at 15,000 rpm.

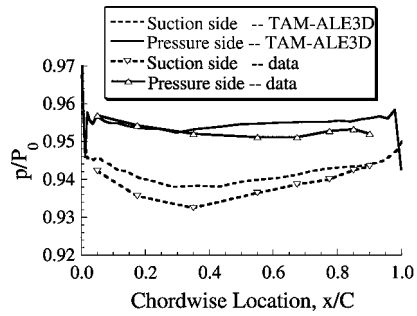

Fig. 5 Time-averaged IGV surface pressure at 15,000 rpm.

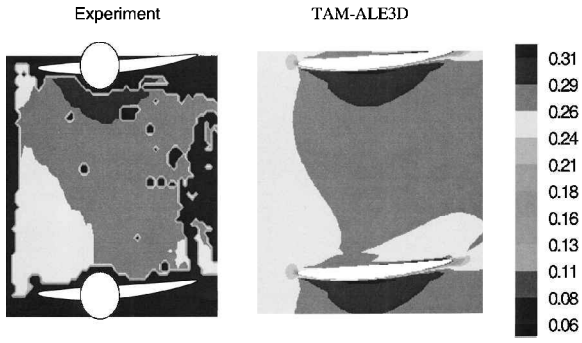

Fig. 6 IGV time-averaged vane-to-vane flow colored by Mach number.

In the Lagrange calculation, the force on the nodes due to the element pressure, q term, and hourglass viscosity is first calculated without accounting for the adjacent domain. These forces, as well as the nodal masses, at the inflow boundary of the downstream domain are then passed to the upstream domain. The linearly interpolated forces and masses from the downstream domain are added to the upstream outflow boundary nodal forces and masses, with the net nodal acceleration calculated by dividing the net nodal force by the net nodal mass. These accelerations are passed to the downstream domain and linearly interpolated to the downstream nodal locations. Finally, Coriolis and centripetal accelerations are added to the accelerations.

For the advection of mass and energy, care is taken to maintain second-order accuracy at the interface between domains. Calculating second-ordered starred quantities for the faces at the interface between domains requires the passing of downwind element quantities from the inflow boundary of the downstream domain to the upstream domain. Similarly, in the downstream domain the interior faces next to the interface between domains require the passing of the upwind-plus-one element quantities from the outflow boundary of the upstream domain to the downstream domain.

The momentum advection calculation at the outflow boundary of the upstream domain is performed without information from the downstream domain. The computed velocities are then passed to the inflow boundary of the downstream domain. These velocities must be interpolated to the downstream nodal positions and then transformed to account for the relative rotation between domains.

Results

The Purdue Transonic Fan features a $1\frac{1}{2}$-stage axial-flow geometry representative of that used in the front stages of advanced aircraft

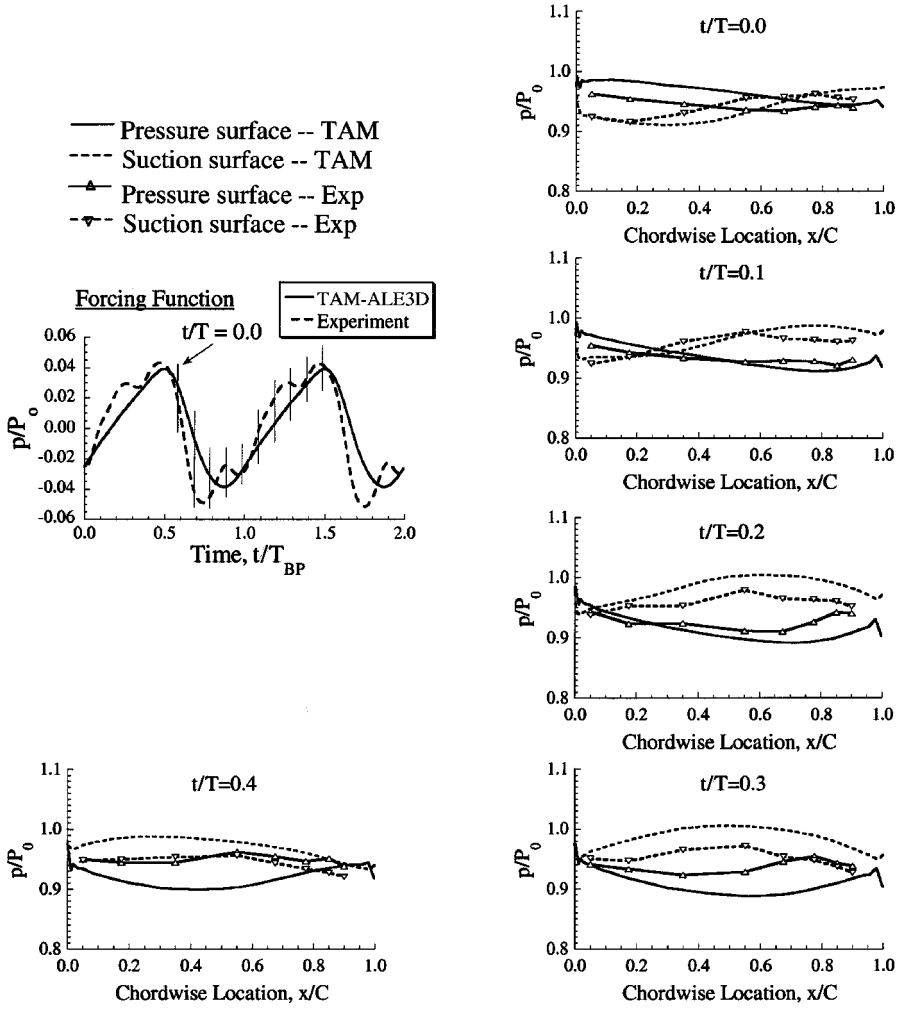

Fig. 7 Time-variant IGV surface pressures at 15,000 rpm, $t/T = 0$–0.4.

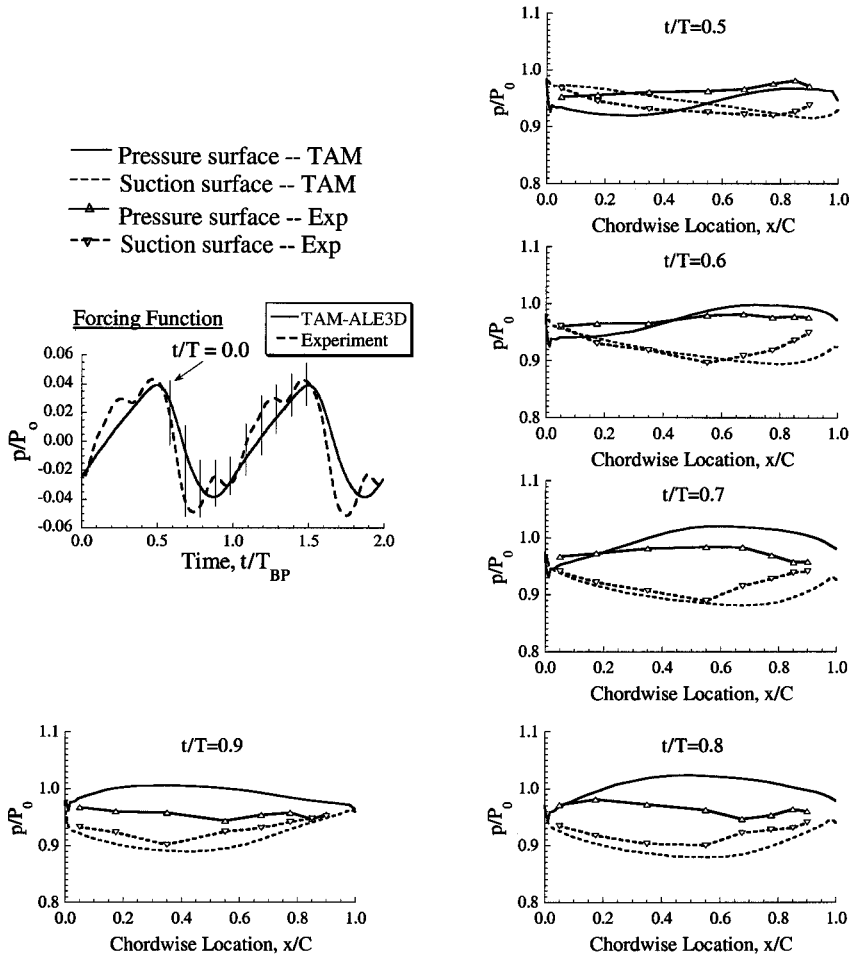

Fig. 8 Time-variant IGV surface pressures at 15,000 rpm, $t/T = 0.5$–0.9.

engine high-pressure compressors. It has a constant hub–tip ratio of 0.667, with a tip diameter of 0.3 m. The IGV row has 18 vanes and the rotor row 19 blades. There is also an 18-vaned stator row downstream of the rotor, but it is not modeled in this study. The IGV profile is an advanced controlled diffusion airfoil design with a 4.45-cm chord and a constant 7% thickness. The rotor blades have a NACA 65 series profile on circular arc meanlines with a 5.08-cm chord and a thickness distribution varying from 10% at the hub to 6% at the tip.

The unsteady flowfield in the IGV passage generated by the downstream rotor has been experimentally investigated at both transonic and subsonic rotor operating conditions.[9,10] Specifically, the unsteady flowfield in the upstream IGV passage generated by the downstream rotor was experimentally investigated at part speed ($N_c = 15{,}000$ rpm) and design speed ($N_c = 20{,}000$ rpm). The potential flow and shock forcing functions to the IGVs were measured with an unsteady static pressure probe, with the resultant 90% span IGV surface unsteady aerodynamic response determined by high-response dynamic pressure transducers. Particle image velocimetry (PIV) measurements quantified the steady and unsteady flow through the IGV passages.

Modeling the $\frac{18}{19}$-airfoil count of the IGV–rotor geometry would require the simulation of the complete annulus. To alleviate this difficulty, the vane count of the IGV row is altered so that IGV and rotor rows each have 19 airfoils, enabling them to be modeled with one passage per row. Increasing the IGV vane count by one changes the geometry of the IGV passage, but does not affect the rotor blade pass period.

Each simulation requires the processing power of two dedicated SGI RS10000 250-MHz CPUs for approximately two weeks. The solution is sufficiently converged when the time-average mass flow rate changes by less than 0.1% from one blade pass period to the next. The time required to change from a uniform flow initial guess to the converged solution is 9 ms, which corresponds to 90,000 time steps.

Mesh

A two-dimensional slice of the IGV and rotor blade passage tip meshes is shown in Fig. 1. Each mesh is an unstructured assembly of hexahedron elements and consists of an O mesh wrapping around the airfoil, with a surrounding H mesh. This configuration gives good resolution around the leading edges while minimizing shearing of the hexahedron elements. The trailing edges of both airfoils are modified to wedges.

There are 26,970 nodes in the IGV mesh, comprising 22,610 hexahedron elements and 1,092 shell elements. The rotor mesh has 29,960 nodes, comprising 24,852 elements and 1,482 shell elements. The shell elements define the airfoil surface and are included in the calculation only as a place to apply the airfoil surface boundary condition for the fluid nodes adjacent to the airfoil. Except for rotor rotation, these shell elements are fixed in space, that is, no airfoil deformation is allowed. There are 19 layers of hexahedron elements in the spanwise direction for both fluid meshes.

Stage Aerodynamic Performance

The predicted aerodynamic performance for the IGV–rotor stage is shown in Fig. 2. The performance data, including the effects of the downstream stator, are also shown. The predicted performance is better than that found experimentally, an expected result because TAM-ALE3D is an inviscid solver. Lacking boundary layers, the simulated flow follows the airfoil profiles more closely, thus allowing more work transfer to the flow. In addition, the data include viscous flow losses from the IGV, rotor, and downstream stator rows, whereas the simulation includes no viscous flow losses.

On the 20,000-rpm operating line in the choked flow region, the simulated mass flow is 2% larger than measured. This is also

attributed to the lack of viscous modeling because the large negative incidences in the choked flow region do not produce separation regions on the rotor pressure side, thus allowing more mass to flow.

In the following results, two data points on the nominal operating line (Fig. 2) are chosen for the TAM-ALE3D simulations because extensive data are available for correlation. The mass flow rates for the simulations are set to match the mass flow rates in the experiments, with the corresponding total pressure ratios differing as noted earlier.

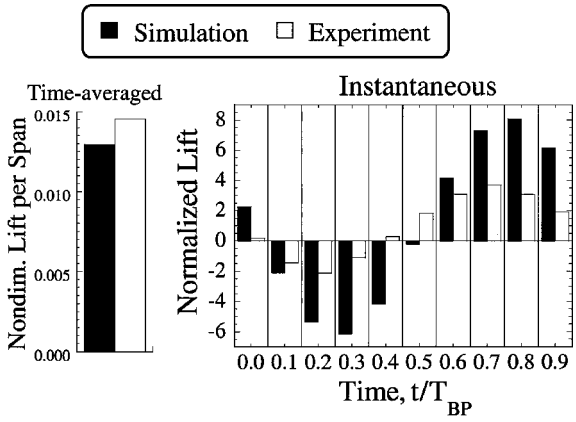

Fig. 9 Time-averaged and time-variant IGV lift per unit span.

Part Speed

Rotor-Generated Forcing

The downstream rotor potential field is the forcing function generating the upstream IGV unsteady aerodynamic response and is determined in both the experiment and the simulation. Experimentally, this is accomplished by an unsteady static pressure probe at 90% span, 21.4% vane chord downstream of the IGV trailing edge, and halfway between vane stacking axes (Fig. 3). Care must be taken when situating an equivalent simulated static pressure probe because the simulation has 19 IGVs, whereas the experiment has 18. The vane surface pressures from both the simulation and experiment are compared on the upper vane. Thus, a simulated static pressure probe is located in the same position relative to the upper vane, that is, 10 deg below the upper vane.

The predicted and measured forcing functions are shown in Fig. 4, with the mean pressure subtracted. The initial vane-blade position at $t = 0$ corresponds to a rotor stacking axis being midway between experimental vane stacking axes, equivalent to the rotor stacking axis being aligned with the static pressure probe. Note that the rotor blade pass frequency is the largest frequency component in both the simulation and experiment. However, the experimental forcing function has a significant higher frequency component at two times

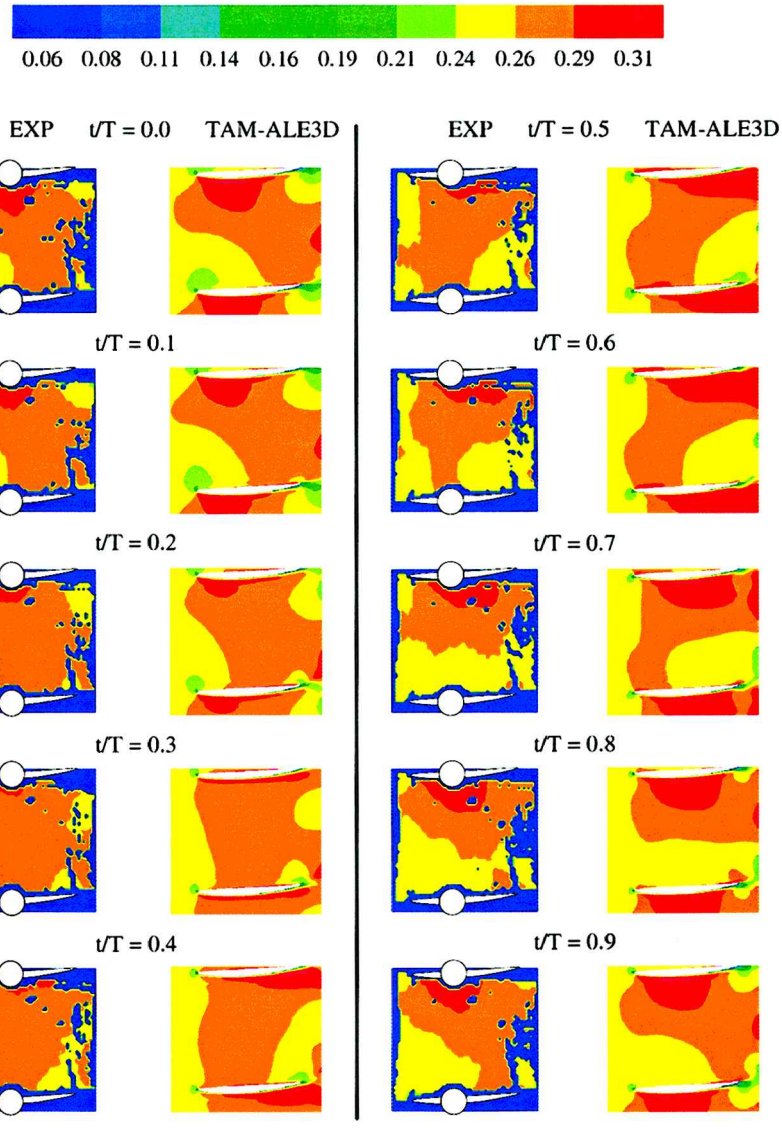

Fig. 10 IGV vane-to-vane flow colored by Mach number at 15,000 rpm.

blade pass frequency. The source of this higher frequency component is unclear, although it could be related to the IGV viscous wake periodically altering the rotor potential field, with this effect not being captured by the inviscid TAM-ALE3D model. Nevertheless, overall agreement between the experimental and simulated forcing function is good.

Time-Averaged Flowfield

The time-averaged IGV surface pressures are shown in Fig. 5. The simulation overpredicts the pressure on the suction side and also on the aft half of the pressure surface. However, this overprediction is slight, never exceeding a 0.6% difference.

The time-averaged vane-to-vane flowfield colored by Mach number is shown in Fig. 6. The dark spots in these PIV data are areas where flowfield information is not resolved due to high flow gradients or laser reflections. The IGV trunnion is also visible in the data, preventing flowfield visualization near the vane at midchord. Note that the IGV vane-to-vane spacing is smaller for the TAM-ALE3D results than for the data because of the increased vane count used in the simulation. There are very similar flowfield structures in the simulated and experimental time-averaged results, with the Mach number increasing in the vane passage due to the blockage of the vanes and a localized high Mach number region evident on the suction side of the IGV.

Instantaneous Flowfield

Both experimental and simulated vane surface pressures are shown at 10 time instants during one rotor blade pass period in Figs. 7 and 8. The relationship between the IGV loading and the pressure just aft of the IGV trailing edge is shown via the forcing function plot in Figs. 7 and 8. Recall that the forcing function probe is located 10 deg below the vane on which the surface pressure data are referred. Thus, the probe's static pressure measurement lags the static pressure aft of the upper vane trailing edge by 0.585 times the blade pass period. The vertical lines in the forcing function denote the expected static pressure directly aft of the IGV 21.4% chord downstream for the times $t/T_{BP} = 0.0$, 0.1, etc., in the surface pressure results.

The trends predicted by TAM-ALE3D and exhibited by the data are similar, but TAM-ALE3D tends to predict larger unsteady pressure fluctuations over the entire IGV chord. In both the prediction and the experiment, the suction side loading begins to be larger than that on the pressure surface over the aft chord starting at $t/T_{BP} = 0.0$. From this time until $t/T_{BP} = 0.5$, the suction side loading is larger than the pressure side loading over most of the chord. At $t/T_{BP} = 0.5$, both predicted and experimental loadings begin to cross over again, with the pressure side loading larger from $t/T_{BP} = 0.6$ to 0.9. Although it appears that the suction side of the vane has higher loading over the majority of the cycle, the vane surface pressure plot of Fig. 4 shows that the pressure side has the higher loading on a time-averaged basis.

The predicted and measured overall lift per unit span experienced by the vane tip at part speed is shown in Fig. 9, with the nondimensional time-averaged lift per unit span shown on the left. The instantaneous lift is normalized by the time-averaged lift, that is, the instantaneous TAM-ALE3D predicted lift by the TAM-ALE3D time-averaged lift and the experimental instantaneous lift by the experimental time-averaged lift.

For the time-averaged lift, TAM-ALE3D predicts 12% less lift than the data. This is partially due to the differing vane counts, that is, the spacing between vanes is 5.3% less for the simulation than for the experiment. A linearized cascade analysis[11] at similar conditions gives a decrease in steady lift of 6% for this same decrease in spacing.

For the instantaneous lift, the magnitude of the simulated lift is often over 100% larger than the measured lift, but the relative phase between the data and the prediction is similar. This large difference in unsteady lift magnitude can also be attributed to the scaling of the geometry in the simulation. In the quasi-three-dimensional study by Micklow et al.,[12] it was found that such scaling to reduce CPU time and storage requirements led to the prediction of greater unsteady interaction effects.

Figure 10 shows the vane-to-vane Mach number field at 10 instants of time during one rotor blade pass period. There is good agreement between the predicted and measured flowfields, with the potential field from the downstream rotor affecting the entire IGV passage flow. A slightly higher Mach number region associated with an acoustic wave is seen to propagate upstream through the IGV passage. This high Mach number region enters the IGV

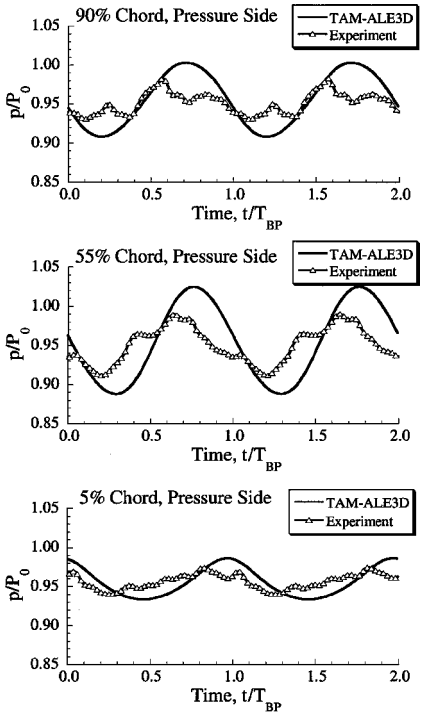

Fig. 11 Vane pressure surface pressures at several chordwise locations, 15,000 rpm.

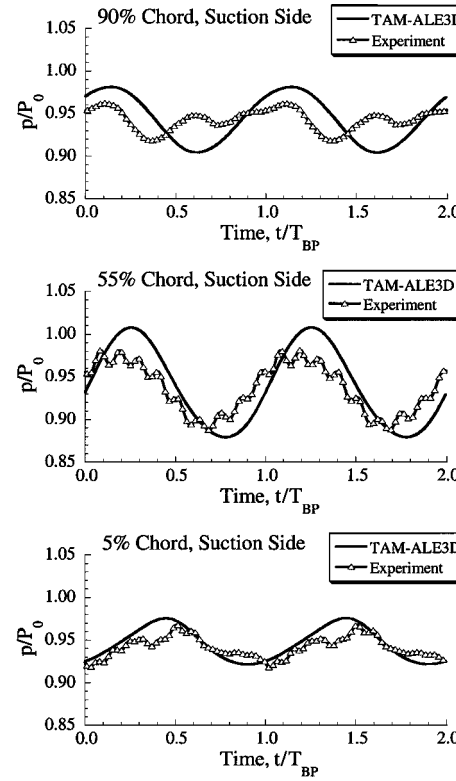

Fig. 12 Vane suction surface pressures at several chordwise locations, 15,000 rpm.

passage at $t/T_{BP} = 0.8$ and continues propagating upstream through the passage until it leaves the IGV passage at $t/T_{BP} = 0.6$. The TAM-ALE3D simulation captures this acoustic disturbance well.

Vane Surface Pressure Time Histories

Figures 11 and 12 show the predicted and measured time variation of the vane surface pressure at several locations along the chord: 5, 55, and 90% chord from the leading edge. The vertical scales in all parts of Figs. 11 and 12 are the same, and so it is evident that the unsteady effects are largest in the midchord region.

The trend of the prediction matches that of the data. There are, however, quantitative differences. The biggest difference is the presence of higher harmonics in the data, whereas only the blade pass frequency is evident in the predictions. The best agreement between prediction and data is at midchord on the suction side of the vane, with the poorest agreement at 90% chord on the suction side. Here, the data have a relatively small blade pass frequency component, whereas the blade pass frequency is dominant in the prediction.

Design Speed

The design-speed flowfield is transonic, with a shock located on the upper-half of the rotor blade. In the simulation, the location of the rotor shock differs from that in the experiment (Fig. 13). Figure 13, drawn to scale, shows the location of the simulated and experimental shock at 90% span at experimental time zero, that is, when the rotor-stacking axis is aligned with the static pressure probe. The rotor shock structure is approximated as a straight line based on the PIV data and the static pressure probe measurement. The simulated shock structure is obtained directly from IGV and rotor flowfield visualization tools. This simulated shock is curved and is located further aft on the rotor.

The differing shock structure between experiment and simulation is not unexpected because the total pressure rise through the rotor is much larger for the simulation. Both simulation and experiment have the same mass flow rate, but the simulation has a total pressure ratio of 1.44, whereas that of the experiment is 1.32.

For the remaining results, the differing shock structure is taken into account by adjusting time zero for the simulation. When time zero is used for the simulation $\frac{2}{10}$ths of a blade pass period later than that in the experiment, both the experimental and simulated shock impact the IGV at the same location and the same time.

Rotor-Generated Forcing

For the design-speed operating point, the predicted and measured forcing functions are shown in Fig. 14, with the mean pressure subtracted. The simulated shock impacts the probe 5% of a blade pass period earlier than the experimental shock. This is consistent with the shock structure shown in Fig. 13 because the simulation time zero has been adjusted to be $\frac{2}{10}$ths of a blade pass period later than experimental time zero. With this adjustment, both shocks impact the IGV at the same time and place, but the curvature of the simulated shock causes it to impact the static pressure probe before the experimental shock.

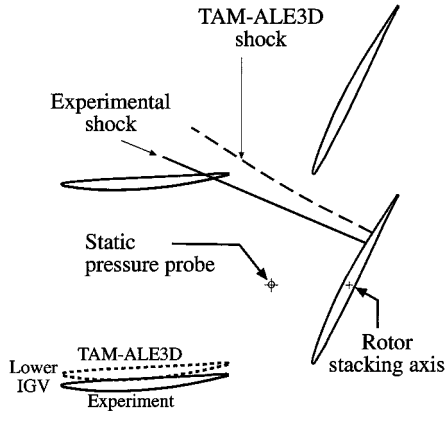

Fig. 13 Experimental and simulated shock location at 90% span time = 0.

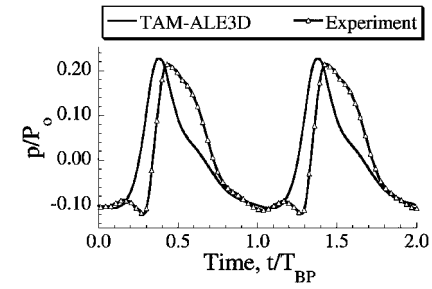

Fig. 14 Rotor-generated forcing function at 20,000 rpm.

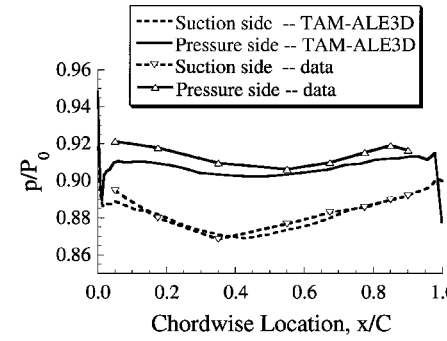

Fig. 15 Time-averaged IGV surface pressure at 20,000 rpm.

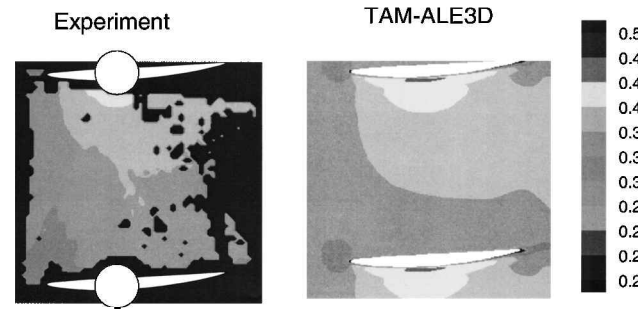

Fig. 16 IGV time-averaged vane-to-vane flow colored by Mach number, 20,000 rpm.

The sawtooth pattern indicative of the shock emanating from the downstream transonic rotor flow is evident in both the prediction and data. The peak-to-peak unsteady forcing function pressure is 30% of the upstream stagnation pressure and is 300% larger than the corresponding unsteady forcing function pressure at part speed.

Time-Averaged Flowfield

The time-averaged IGV surface pressures for simulation and experiment are shown in Fig. 15. The prediction and data are very close over the suction side. Over the pressure side of the vane, the prediction underpredicts the pressure, with the maximum difference between prediction and data being 1.2%, near the leading edge.

The time-averaged vane-to-vane flowfield colored by Mach number is shown in Fig. 16. There are very similar flowfield structures in the simulated and experimental time-averaged results, with a high Mach number region evident on the suction side of the IGV. Within the passage, the simulation has a slightly higher Mach number. This is expected because the increased vane count creates more blockage, and, thus, higher velocities through the passage are required for the same mass flow rate.

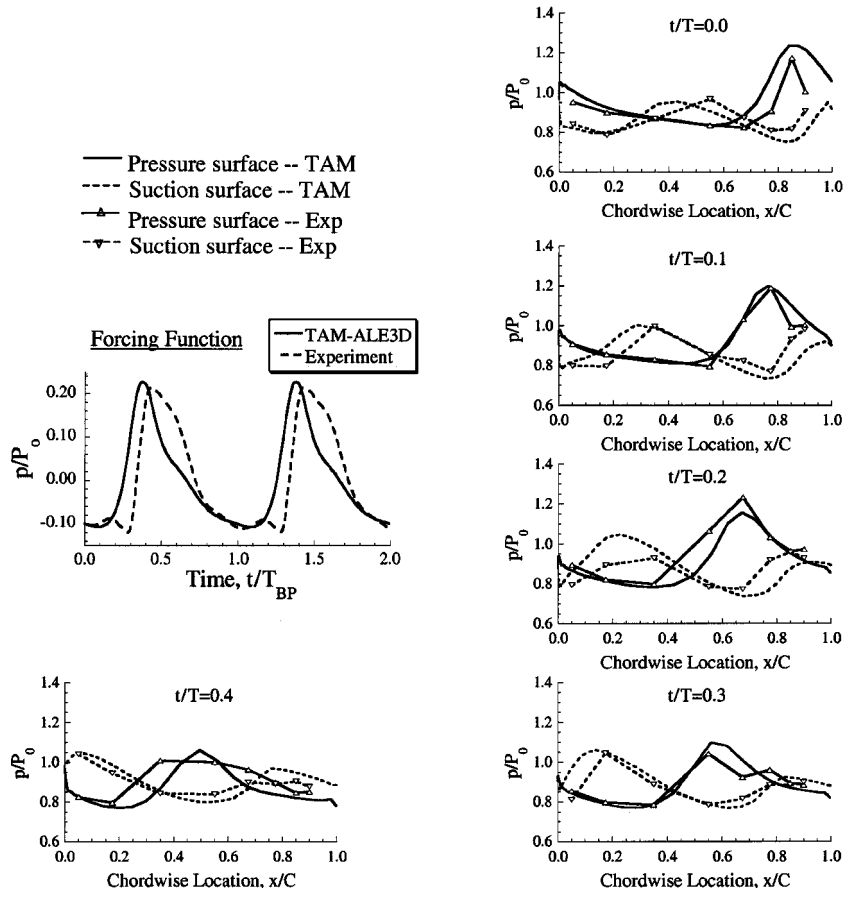

Fig. 17 Time-variant IGV surface pressures at 20,000 rpm, $t/T = 0$–0.4.

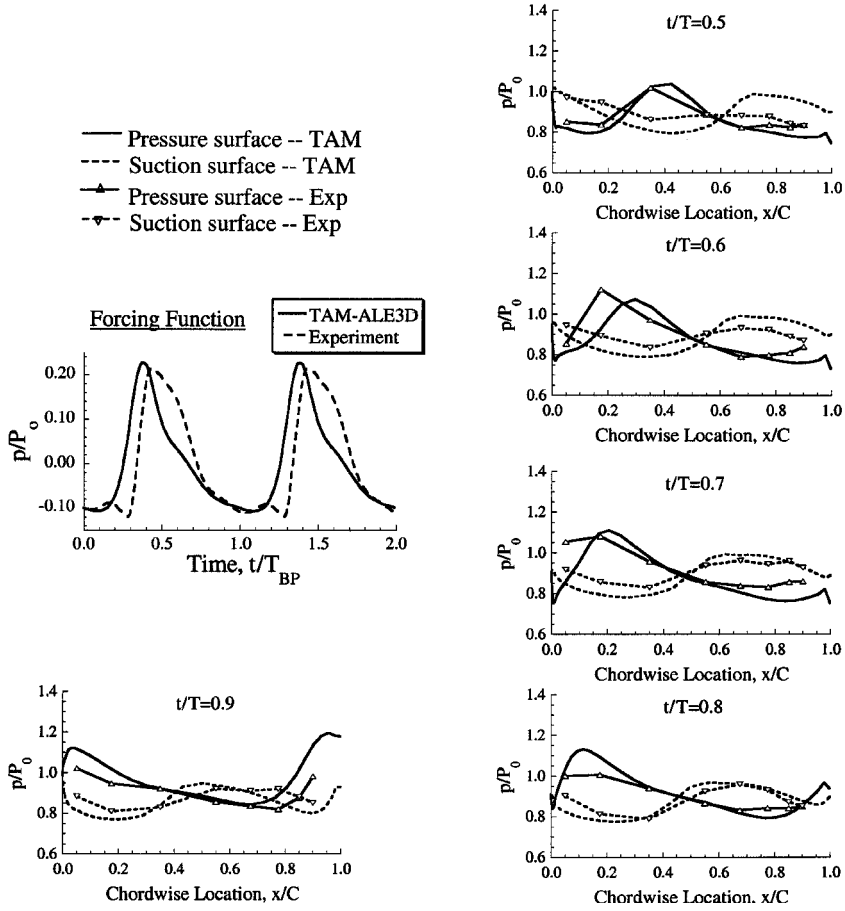

Fig. 18 Time-variant IGV surface pressures at 20,000 rpm, $t/T = 0.5$–0.9.

Instantaneous Flowfield

The vane tip time-variant loading, including comparison to data, is presented in Figs. 17 and 18. There is a large disturbance propagating upstream along the chord that produces pressure differences along the chord of as much as 40% of the freestream stagnation pressure. This large disturbance is due to the downstream shock emanating from the rotor traveling upstream and impacting the IGV. The agreement between the TAM-ALE3D prediction and the experiment is good, with TAM-ALE3D predicting the shape and magnitude of the disturbance very well.

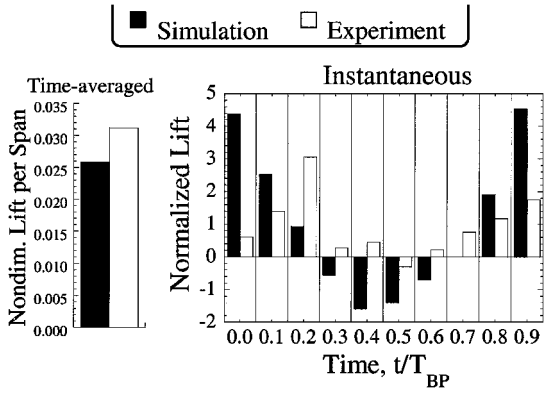

Fig. 19 Time-averaged and time-variant IGV lift per unit span at 20,000 rpm.

The predicted and measured overall lift per unit span experienced by the vane tip is presented in Fig. 19, with these lifts normalized as before. The time-averaged lift prediction is 19% lower than the data, which is partially explained by the geometry scaling. With regard to the instantaneous lift, first note that the differences between the instantaneous time-averaged lift are smaller at design speed than at part speed. This is understood by noting that the instantaneous lift is proportional to the area between the suction side and pressure side loading curves vs chord. Because of the large variations in IGV loading along the chord at design speed, the net area between the curves varies relatively little from one time to the next. In contrast, at part speed, the loading varies relatively slowly along the chord. Thus, although these curves do not have localized loadings as large as at design speed, the total area between the suction and pressure side curves, that is, the lift, becomes relatively large. Thus, in terms of net lift on the vane, part speed has more unsteadiness than does the design-speed condition. However, in terms of localized loadings along the chord, the design-speed flow produces more unsteadiness.

The predicted and measured instantaneous lift differ significantly at times and are in good agreement at times, with the best agreement at $t/T_{BP} = 0.1$ and 0.8. This is associated with the large pressure variations along the chord. Namely, with the large spatial variations in the surface instantaneous loading, small variations can cause large differences in the instantaneous lift. Hence, very accurate unsteady

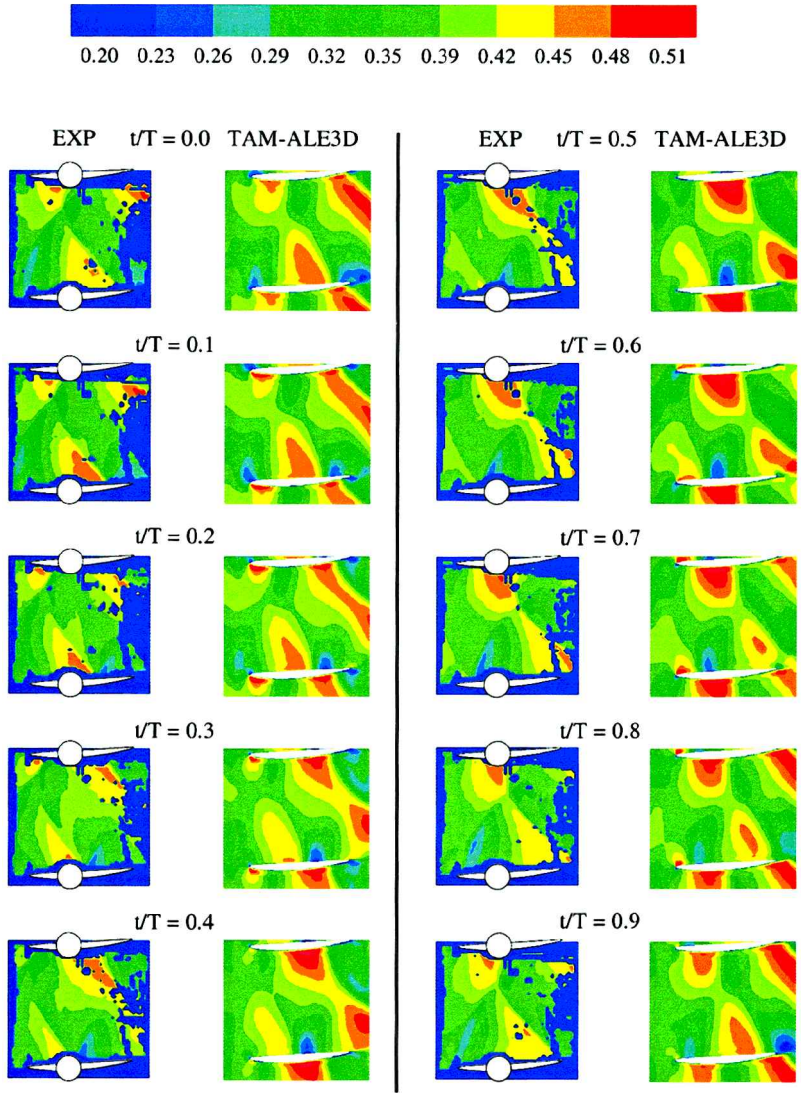

Fig. 20 IGV vane-to-vane flow colored by Mach number at 20,000 rpm.

pressure predictions are necessary to predict the instantaneous lift accurately. Specifically, the simulated lift tends to follow a simple sinusoidal pattern in time. In contrast, the data have a more complicated time history, containing significant higher harmonic contributions.

Figure 20 shows the Mach number field at 10 time instants during one rotor blade pass period. The strong shock from the transonic downstream rotor, indicated by the dark green regions just aft of the high Mach number red regions, is seen to propagate through the IGV passage. At $t/T_{BP} = 0.0$, the shock impacts the IGV trailing edge. The shock reflection by the IGV pressure surface at later times causes a large increase and then a large decrease in Mach number along this surface. This large gradient region propagates upstream along the pressure surface until it reaches the IGV leading edge at $t/T_{BP} = 0.8$ and exits the vane passage. The reflected shock on the pressure surface makes an angle equal and opposite to the incident shock angle and, thus, angles back toward the downstream direction. When started at $t/T_{BP} = 0.2$, this reflected shock breaks the high Mach number region in the middle of the passage into two parts. The simulation shows excellent agreement with the data in the context of these highly complex flow phenomena.

Blade Surface Pressure Time Histories

Figures 21 and 22 show the predicted and measured time variation of the vane surface pressure at locations 5, 55, and 90% chord from the leading edge. Note that the variation in pressure on the vane pressure side is much larger than on the suction side. On both suction and pressure sides, a significant difference between the prediction and the data is the higher harmonics in the data.

On the vane pressure side, the movement of a large pressure disturbance is evident over the entire chord. This is the incident shock and its reflection propagating from downstream to upstream. The peak in pressure in the simulation and experiment occurs at a similar time at 90% chord. However, this pressure pulse appears to move upstream more slowly in the simulation than in the experiment. The magnitude of this peak is similar between experiment and simulation at 90% chord, but at 55% chord the simulation peak drops approximately 15%, whereas the experimental peak remains

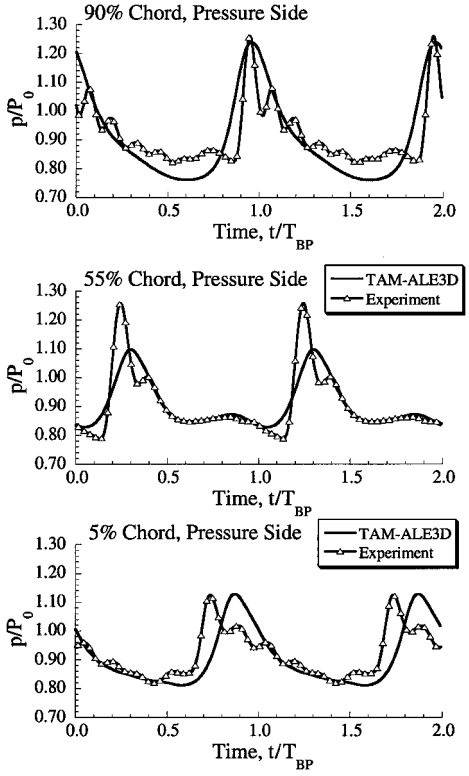

Fig. 21 Predicted and measured vane surface pressures at several chordwise locations, 20,000 rpm.

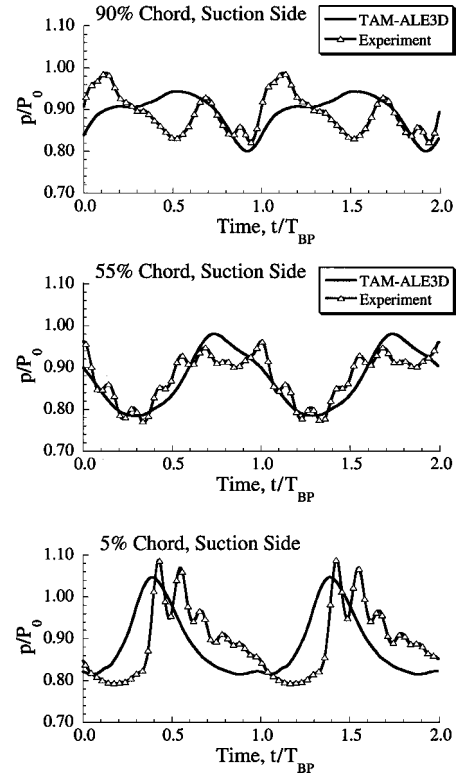

Fig. 22 Predicted and measured vane surface pressures at several chordwise locations, 20,000 rpm.

the same. Between 55 and 5% chord, the experimental peak drops 15%, the simulated peak remains about the same, and so they have approximately equal magnitude at 5% chord.

On the vane suction side there is poor agreement between experiment and simulation at 90% chord. This could be attributed to inadequate mesh resolution in the trailing-edge region. Surprisingly, the agreement improves at 55 and 5% chord. Both in the experiment and in the simulation, the suction side disturbance increases in strength as it moves from trailing edge to leading edge.

Numerical Accuracy

A mesh resolution study was performed at part-speed conditions to evaluate the accuracy of the TAM-ALE3D solution. Three mesh sizes were used: 1) 27,534 nodes with 11 elements spanwise, 2) 56,930 nodes with 19 elements spanwise (used throughout this paper), and 3) 122,813 nodes with 23 elements spanwise, where the node number totals include both IGV and rotor meshes. As the number of nodes increases, the time-averaged lift decreases from 0.0141 to 0.0130 to 0.0125. However, the unsteady forcing function and unsteady lift show only negligible variation in both magnitude and phase. Other details of the flowfield, such as the trailing-edge time-variant pressures, were not investigated.

Summary

Multistage turbomachinery analyses are necessary in designing for reliability, especially in the realm of HCF. Multistage analyses are able to capture the blade row interacting and coupling effects, which is crucial for predicting the life of blades operating in the highly unsteady turbomachinery environment. As part of the development of these multistage analyses, it is crucial that they be validated with data.

The TAM-ALE3D finite element code has been parallelized and extended to model multistage turbomachinery flows. This Euler analysis is applied to an IGV–rotor configuration for which state-of-the-art data are available. In this configuration, potential and shock effects generated by the downstream rotor cause significant unsteadiness on the upstream IGVs.

For both subsonic and transonic rotor operating conditions, the time-averaged flow was predicted well by the simulation. The

predicted instantaneous flowfield compares well to the data at part speed, but at design speed the location of the shock is predicted to be aft of its location in the experiment. Despite this difference, on adjusting simulation time zero, the behavior of the shock within the IGV passage, including its complex reflections and interactions, are predicted well.

Quantitative measurements of IGV lift for both subsonic and transonic rotor conditions show room for improvement. In the subsonic case, the unsteady lift follows a sinusoid in both the experiment and simulation. However, the simulation overpredicted the unsteady lift magnitude by 100%. In the transonic case, the simulated IGV lift did an inadequate job of tracking the data and lacked the data higher harmonics.

Two sources of error in the simulation are the geometry scaling for rows with equal airfoil counts and the lack of viscous effects.

Acknowledgments

This research was sponsored, in part, by the Air Force Office of Scientific Research and the Department of Energy ASCI Program Contract LG-6982. This support is most gratefully acknowledged.

References

[1]Janus, M. J., Horstman, H. Z., and Whitfield, D. L., "Unsteady Flowfield Simulation of Ducted Prop-Fan Configurations," AIAA Paper 92-0521, 1992.

[2]Janus, M. J., and Whitfield, D. L., "Simple Time-Accurate Turbomachinery Algorithm with Numerical Solutions of an Uneven Blade Count Configuration," AIAA Paper 89-0206, 1989.

[3]Hall, E. J., Topp, D. A., Heidegger, N. J., McNulty, G. S., Weber, K. F., and Delaney, R. A., "Task 7—Endwall Treatment Inlet Flow Distortion Analysis Final Report," NASA CR-195468, May 1996.

[4]Gottfried, D. A., and Fleeter, S., "Prediction of Unsteady Cascade Aerodynamics by an Arbitrary Lagrangian–Eulerian Finite Element Method," AIAA-98-3746, July 1998.

[5]Noh, W. F., "Numerical Methods in Hydrodynamic Calculations," Lawrence Livermore National Lab., Univ. of California, Livermore, CA, Rept. UCRL-52112, June 1976, pp. 49–58.

[6]Gottfried, D. A., and Fleeter, S., "Aerodynamic Damping Predictions for Turbomachine Blade Rows Using a Three-Dimensional Time Marching Simulation," AIAA Paper 99-2810, June 1999.

[7]Gottfried, D. A., "Simulation of Fluid–Structure Interaction in Turbomachines," Ph.D. Dissertation, School of Mechanical Engineering, Purdue Univ., West Lafayette, IN, May 2000, pp. 22–24 and 41, 42.

[8]Giles, M. B., "Nonreflecting Boundary Conditions for Euler Equation Calculations," *AIAA Journal*, Vol. 28, No. 12, 1989, pp. 2050–2058.

[9]Sanders, A. J., and Fleeter, S., "Experimental Investigation of Inlet Guide Vane–Rotor Interactions in a Transonic Axial-Flow Compressor," AIAA Paper 98-3291, 1998.

[10]Sanders, A. J., Papalia, J., and Fleeter, S., "Particle Image Velocimetry Investigation of Rotor–Inlet Guide Vane Interactions in a Transonic Axial-Flow Compressor," AIAA Paper 99-2674, 1999.

[11]Smith, S. N., "Discrete Frequency Sound Generation in Axial Flow Turbomachines," Univ. Engineering Dept., R&M 3709, Cambridge Univ., Cambridge, England, U.K., March 1972.

[12]Micklow, G. J., Sauve, J. P., and Shivaraman, K., "Numerical Simulations of Advanced Transonic Compressor Stages Using an Unsteady Quasi-Three-Dimensional Flow Solver," American Society of Mechanical Engineers, ASME Paper 95-GT-440, 1995.